Received: 27 May 2019 | Revised: 18 June 2019 | Accepted: 22 June 2019

DOI: 10.1002/hbm.24705

RESEARCH ARTICLE

WILEY

Exploring the functional connectome in white matter

Jiao Li[1,2] | Bharat B. Biswal[1,2,3] | Pan Wang[1,2] | Xujun Duan[1,2] | Qian Cui[4] | Huafu Chen[1,2] | Wei Liao[1,2]

[1]The Clinical Hospital of Chengdu Brain Science Institute, MOE Key Laboratory for Neuroinformation, University of Electronic Science and Technology of China, Chengdu, China

[2]School of Life Science and Technology, Center for Information in BioMedicine, University of Electronic Science and Technology of China, Chengdu, China

[3]Department of Biomedical Engineering, New Jersey Institute of Technology, Newark, New Jersey

[4]School of Public Administration, University of Electronic Science and Technology of China, Chengdu, China

Correspondence
Huafu Chen and Wei Liao, The Clinical Hospital of Chengdu Brain Science Institute, MOE Key Laboratory for Neuroinformation, University of Electronic Science and Technology of China, Chengdu 610054, China.
Email: chenhf@uestc.edu.cn (H. C.) and
Email: weiliao.wl@gmail.com (W. L.)

Funding information
National Natural Science Foundation of China, Grant/Award Numbers: 61533006, 61871077, U1808204, 81771919, 61673089; "111" Project, Grant/Award Number: B12027; Sichuan Science and Technology Program, Grant/Award Number: 2018TJPT0016; China Postdoctoral Science Foundation, Grant/Award Number: 2013M532229

Abstract

A major challenge in neuroscience is understanding how brain function emerges from the connectome. Most current methods have focused on quantifying functional connectomes in gray-matter (GM) signals obtained from functional magnetic resonance imaging (fMRI), while signals from white-matter (WM) have generally been excluded as noise. In this study, we derived a functional connectome from WM resting-state blood-oxygen-level-dependent (BOLD)-fMRI signals from a large cohort (n = 488). The WM functional connectome exhibited weak small-world topology and non-random modularity. We also found a long-term (i.e., over 10 months) topological reliability, with topological reproducibility within different brain parcellation strategies, spatial distance effect, global and cerebrospinal fluid signals regression or not. Furthermore, the small-worldness was positively correlated with individuals' intelligence values (r = .17, $p_{corrected}$ = .0009). The current findings offer initial evidence using WM connectome and present additional measures by which to uncover WM functional information in both healthy individuals and in cases of clinical disease.

KEYWORDS
functional connectome, network topology, resting-state, topological reliability, white matter

1 | INTRODUCTION

In general, brain networks can be derived from structural connectivity (anatomy), functional connectivity (statistical dependencies), and even effective connectivity (causal relations) among collections of distributed brain regions (Bullmore & Sporns, 2009; Sporns, 2012). Functional networks can be calculated using temporal correlations—or coherences—between blood oxygen level-dependent (BOLD)–functional magnetic resonance imaging (fMRI) signals from distinct brain regions in gray-matter (GM) (Achard, Salvador, Whitcher, Suckling, & Bullmore, 2006; Biswal et al., 2010; Biswal, Yetkin, Haughton, & Hyde, 1995). It has been suggested that human brain networks are organized to allow optimized efficiency, which implies a small-world topology, a densely connected core of high-degree hubs, and a modular organization (Avena-Koenigsberger, Misic, & Sporns, 2017). Investigations into such an organization serve to uncover fine details concerning the brain's network architecture. However, previous studies that have evaluated GM functional networks have both underappreciated and failed to provide direct evidence for the presence of functional information in white-matter (WM).

The role of WM in neuroimaging remains controversial. Historically, BOLD-fMRI hemodynamic responses have been considered

noisy, unreliable and undetectable in WM. In recent years, however, brain activation in WM has been detected using BOLD-fMRI (Gawryluk, Mazerolle, & D'Arcy, 2014). Mounting evidence from the interhemispheric transfer task as well as the Poffenberger and the Sperry paradigms support for the already well-established example using fMRI activation in WM that is implicated in the corpus callosum and internal capsule (Courtemanche, Sparrey, Song, MacKay, & D'Arcy, 2018; D'Arcy, Hamilton, Jarmasz, Sullivan, & Stroink, 2006; Gawryluk, Mazerolle, Beyea, & D'Arcy, 2014; Gawryluk, Mazerolle, Brewer, Beyea, & D'Arcy, 2011; Tettamanti et al., 2002). In addition, neural activity actually elicits temporal and spectral profiles of hemodynamic responses in WM that are similar to those in GM under visual stimulation (Ding et al., 2013, 2016; Huang et al., 2018). Recently, we examined whether the power of low-frequency BOLD fluctuations in WM during resting state exhibits a specific distribution rather than a random distribution of noise at rest (Ji, Liao, Chen, Zhang, & Wang, 2017). Moreover, this WM activity, which is estimated from low-frequency BOLD fluctuations, was shown to be modulated under different cognitive tasks (Huang et al., 2018; Ji, Liao, Chen, Zhang, & Wang, 2017; Marussich, Lu, Wen, & Liu, 2017; Wu et al., 2017). When combined, these findings converged to provide evidence of neural activation/activity in WM based on task-related/free BOLD-fMRI (Gawryluk, Mazerolle, & D'Arcy, 2014) and showed that fMRI is a promising tool for investigating WM functioning in the human brain.

While previous studies have investigated WM activation/activity, we wanted to explore functional connectivity in WM by examining functional networks in WM. For instance, as the specific WM tracts are tracked using diffusion data, it is also possible to identify functional connectivity in anatomical bundles with resting-state fMRI data (Ding et al., 2018; Marussich et al., 2017; Wu et al., 2017). Recently, Peer et al. demonstrated that WM also had an intrinsic functional organization, indicating interacting networks of functional modules as seen in a resting-state fMRI investigation and that were similar to those found in GM functional networks (Peer, Nitzan, Bick, Levin, & Arzy, 2017). In line with this work, the perception-motor functional network in WM was found to be abnormal in schizophrenia (Jiang et al., 2019). More recently, Ji et al. found that patients with Parkinson's disease showed increased small-worldness in the WM functional network (Ji et al., 2019). Moreover, brain function profiles of WM function, including power spectra, coupling of WM and GM functional connectivity were found to be disrupted in various brain disorders, such as pontine stroke, Alzheimer's disease, and epilepsy (Jiang et al., 2019; Makedonov, Chen, Masellis, & MacIntosh, 2016; Wang et al., 2019). However, such previous studies focused on the extant functional modules and large-scale networks in WM; used relatively small sample sizes; and failed to offer direct evidence for the different roles played by functional connectomes within WM and GM.

In the present study, we explored the resting-state WM functional connectome in a large cohort of healthy controls (n = 488). We utilized graph theoretical analysis, which had been successfully applied to an association matrix of functional connectivity measures (Liao et al., 2018). We investigated the following: (a) whether the WM functional connectome has features of complex networks, such as a small-world topology, densely connected hubs, or modular organization; (b) in the case that the WM functional connectome showed typical network architectures, whether any differences of brain architectures or mechanisms were found between WM and GM functional connectomes; and (c) whether these brain architectures were reliable over a long-term (over 10 months) period in healthy controls (Time 1 and Time 2: n = 175).

2 | MATERIALS AND METHODS

2.1 | Subjects

Test–retest data was obtained from a large longitudinal cohort, namely, Southwest University Longitudinal Imaging Multimodal (SLIM) study. For detailed description about the subject information and data acquisition parameters, please see Liu et al. (2017). The data is available for research purposes through the International Data-sharing Initiative (http://fcon_1000.projects.nitrc.org/).

The above-mentioned data was obtained from healthy subjects (n = 558, 305 females; aged between 18 and 27 years; age (mean ± SD) 20.08 ± 1.28 years) who were recruited from Southwest University, Chongqing, China. This study was approved by the Institutional Human Participants Review Board of the Southwest University Imaging Center. Written informed consent was obtained from all subjects. Subjects were excluded if they: (a) were < 18 years of age; (b) had been diagnosed with psychiatric or neurological disorders; (c) had used psychiatric drugs within the 3 months prior to scanning; (d) were pregnant; (e) had a history of head trauma; (f) had metal devices such as electronic implants; or (g) met the DSM-V criteria for any psychiatric disorders. Nine months after the first scanning session (Time 1), 221 subjects were requested to undergo a follow-up scanning (Time 2). Scans for each subject were separated by an average of 10.4 ± 3.61 (mean ± SD) months.

2.2 | Data acquisition

All subjects underwent structural and functional imaging scanning using a Siemens Trio 3.0 T scanner at Southwest University, Chongqing, China. The T1-weighted anatomical images (repetition time = 1,900 ms, echo time = 2.52 ms, flip angle = 9°, field of view = 256 × 256 mm^2, matrix = 256 × 256, voxel size = 1 × 1 × 1 mm^3, slices = 176) were acquired. Subsequently, resting-state BOLD-fMRI were acquired using a single-shot, gradient-recalled echo planar imaging sequence (repetition time = 2,000 ms, echo time = 30 ms, flip angle = 90°, field of view =220 × 220 mm^2, matrix = 64 × 64, voxel size = 3.4 × 3.4 × 3 mm^3, slices = 32). For each subject, a total of 242 volumes (484 s) were acquired. All subjects were instructed to simply rest with their eyes closed.

2.3 | Data preprocessing

Functional images were preprocessed using the DPARSF (v4.3, www.restfmri.net) and SPM12 toolkits (www.fil.ion.ucl.ac.uk/spm/

software/spm12). Slice-timing correction and realignment were applied to the 235 functional volumes after excluding the first 7 volumes (14 s). Subjects were excluded if the head motion exceeded 2.0 mm translation or 2.0° rotation. The mean framewise-displacement (FD) was also calculated for each subject.

Structural images were then co-registered with the preprocessed functional images (mean functional image for each subject), and segmented into GM, WM, and cerebrospinal fluid (CSF) using a diffeomorphic nonlinear registration algorithm (DARTEL; Ashburner, 2007) in SPM12. Briefly, DARTEL works by aligning GM across images, while simultaneously aligning WM. This procedure generates its own increasingly crisp average template images for a group, to which images are iteratively aligned (Ashburner & Friston, 2009). We used the default parameter setting. Specifically, for bias regularization, the parameters were set to light regularization (0.001); while bias full width at half maximum (FWHM) was set at a 60 mm cutoff. This procedure a generates WM and GM files, a series of template images, and segment parameters.

To minimize mixing signal (and noise) components from the WM and GM regions due to partial volume effect, subsequent processing of the functional images was performed separately for WM and GM, in accordance with our previous study parameters (Ji, Liao, Chen, Zhang, & Wang, 2017). First, individual masks were generated using a rigorous 90% threshold on the probability maps of both WM and GM (i.e., produced by structural segmentation), respectively. Second, functional images were spatially separated into WM and GM images using the dot product between functional images and the two masks (i.e., WM and GM). Third, the mean CSF signals (95% thresholded), 24 head motion parameters (six head motion parameters, one time point before, and the 12 corresponding squared items), and scrubbing parameters (FD > 0.5 mm along with one-forward and two-back neighbors) were regressed out from functional data (Liao et al., 2019). To avoid elimination of important neural signals, we did not remove or regress out WM or global signals (Huang et al., 2018; Ji, Liao, Chen, Zhang, & Wang, 2017; Peer et al., 2017).

Next, the segmented WM and GM structural images were spatially normalized onto Montreal Neurological Institute (MNI) space using deformation fields from DARTEL. Specifically, the DARTEL template was set as the final iterative template images (usually called Template_6.nii). This template is registered to MNI space (affine transform), and generates deformation fields. Thus, the WM and GM functional images under the WM and GM masks are also normalized to MNI space using these deformation fields, and are resampled to $3 \times 3 \times 3$ mm^3. Then, only voxels identified as WM or GM across 80% of subjects were included as part of the group-level WM or GM masks. To exclude the impact of deep brain structures, the probability (25% threshold) Harvard-Oxford Atlas was used to remove subcortical nuclei (i.e., bilateral thalamus, putamen, caudate, pallidum, and nucleus accumbens) from the group-level WM and GM masks. To minimize spurious local spatial correlations between voxels, spatial smoothing was not applied. Subsequently, linear trending and band-pass filtering (0.01–0.10 Hz) was performed to minimize any drifts as well as minimize high frequency physiological noise sources such as the respiration rate. Finally, as functional connectivity is sensitive to the confounding factor of head motion, scrubbing regression was performed to reduce any spurious correlations (Power, Barnes, Snyder, Schlaggar, & Petersen, 2012). If the FD of a point exceeded 0.5 mm, the value of the signal at the point, as well as one forward and two back neighbors were removed. Subjects with 80% of their volumes remaining were included for further analysis.

2.4 | Exclusion criteria

First, we excluded subjects whose head motion exceeded 2.0 mm of translation or 2.0° of rotation, and whose remaining volumes were less than 80% after scrubbing analysis. In this study, 47 subjects out of a total of 558 subjects were excluded and no further analysis was performed. The quality of preprocessed functional images was then checked, excluding an additional 23 subjects with low quality functional images (e.g., most part of the temporal lobe was uncovered) from remained 511 subjects. Finally, 488 subjects were included in Time 1, and 175 subjects were included in the test–retest analysis (Time 1 and Time 2).

2.5 | Construction of the WM functional connectome

The group-level WM mask was subdivided into 128 random regions of interest (ROIs) and was generated and approximately identical in size (mean ± *SD* = 143 ± 6 voxels across ROIs), as previously described by Zalesky et al. (2010). To ensure the equality of sequential comparison analysis, we first split the WM and GM masks into half across hemispheres, and then divided each half mask in 64 random ROIs using the region-growing method (Zalesky et al., 2010). The WM group parcellation (WM.nii) used here is attached as Supporting Information Data S1. Following construction of the WM functional connectome, correlation matrices (128×128) were produced using Pearson's correlation coefficient between each ROI's averaged time series. Fisher's *r* to *Z* transformation was applied to each of the correlation matrices. A schematic of the analyses is shown in Figure 1. Finally, we estimated the topological properties of the WM functional connectome.

2.6 | Network properties of the WM functional connectome

2.6.1 | Threshold selection

To explore the influence of thresholding on topological properties (Bullmore & Bassett, 2011), we used sparsity-based (proportional) thresholding to the weighted correlation matrix corresponding to each subject (Garrison, Scheinost, Finn, Shen, & Constable, 2015). The sparsity was defined as the ratio of the real edge numbers divided by the maximum possible edge numbers in a given network at a r_{thr}. We decreased the r_{thr} from 1 to 0 (from maximum to minimum) till the existing number of edges satisfies a sparsity threshold. Specifically,

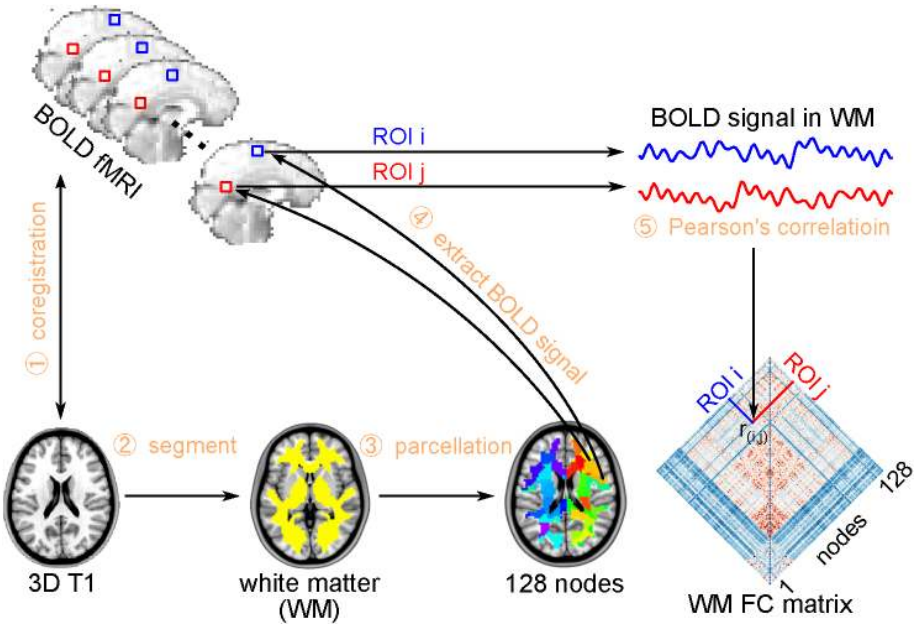

FIGURE 1 Construction of white-matter (WM) functional connectome. Step 1: Structural image (3D T1) was co-registered with the preprocessed functional images (mean functional image). Step 2: The co-registered 3D T1 image was segmented into white-matter (WM), gray-matter (GM), and CSF. Step 3: The group-level WM mask was then divided into 128 random ROIs (nodes) of an approximately identical size. Step 4: Functional images were then spatially separated into segmented WM. After sequent preprocessing, only functional voxels identified as WM across 80% subjects were included as part of the group-level WM mask. Next, BOLD-fMRI signals of each ROI was extracted by averaging all voxels' time series in the node. Step 5: A correlation matrix was produced using Pearson's correlation coefficient between any paired node's averaged time series for each subject. BOLD-fMRI, blood-oxygen-level-dependent functional magnetic resonance imaging; CSF, cerebrospinal fluid; ROI, region-of-interest [Color figure can be viewed at wileyonlinelibrary.com]

$$0 \le \text{sparsity} \le 1 = \frac{\varepsilon_{r_{thr}}}{N(N-1)/2}$$

where $\varepsilon_{r_{thr}}$ expresses the existing number of edges generated by thresholding at r_{thr}, and $N(N-1)/2$ represents the maximum possible number of edges existing in a given network of N nodes (Bullmore & Bassett, 2011; Liao et al., 2018). In this case, when $r_{thr} = 0$, sparsity = 1; when $r_{thr} = 1$, sparsity = 0.

The minimum sparsity was defined across all subjects as follows: (a) the mean degree of a node (the number of connections to the node) over all nodes in thresholded weighted matrices was greater than $2 \times \log(N) \approx 9.7$ (Achard & Bullmore, 2007; Ji et al., 2017; Liao et al., 2011, 2018); where N expresses the number of nodes, $N = 128$. In this case, total number of edges ≈882, which was equivalent to sparsity = 0.11 or 11% of the maximum number of edges possible ($C^2_{128} = 8128$) in a network of 128 nodes. This procedure allowed us to estimate small-world properties (He, Chen, & Evans, 2007), and to compare the topological properties of brain networks to those of equally-sized random networks with a minimum mean degree >log(N), in order to guarantee that a given random graph will be connected (Watts & Strogatz, 1998). (b) The above-mentioned sparsity was further adjusted to ensure that the size of the giant connected cluster, or largest subgraph, was greater than 80% of the total number of nodes in the network ($N \times 80\% \approx 103$). The maximum sparsity corresponds to the lowest significant correlation coefficients $p < .05$ for all WM or GM weighted matrices across all subjects (Ji et al., 2017). We counted the remaining edges after thresholding ($p < .05$) for the weighted matrix of each subject, which results in maximum sparsity (the remaining edges divided by the maximum possible edges) for that subject. This procedure minimizes the number of spurious edges (Ji et al., 2017; Liao et al., 2018). As such, a range of sparsity thresholds (WM functional network: 0.17–0.42, interval = 0.01; GM functional network: 0.11–0.48, interval = 0.01) could be pre-selected.

2.6.2 | Global topological properties

The global topological properties of WM and GM functional connectomes were computed using Gretna software (v2.0, www.nitrc.org/projects/gretna). The following parameters were included the network strength (S), global efficiency (E_{glob}), local efficiency (E_{loc}), normalized clustering coefficient (γ), normalized shortest path length (λ), and small-worldness (σ). A review outlines the uses and interpretations of these topological properties (Rubinov & Sporns, 2010). Briefly, S measures the connectivity capacity of the entire network. E_{glob} quantifies the capacity of information exchange across the whole network, where information is concurrently transferred (Latora & Marchiori, 2001). E_{loc} can be regarded as a measure of the fault tolerance of the subgraph, showing how efficiently information is exchanged at the local level. Small-worldness supports both segregated and integrated information processing. The mathematical definitions of these topological properties are listed in the Supporting Information Data S2.

2.6.3 | Generation of random networks

Brain networks are always compared to random networks to validate its nonrandom topology. As suggested by Stam et al., statistical comparisons should generally be performed between networks that have equal (or at least similar) degree sequence (Stam, Jones, Nolte, Breakspear, & Scheltens, 2007). In line with previous studies (Maslov & Sneppen, 2002; Sporns & Zwi, 2004), a Markov-chain algorithm was used to generate random networks by ensuring the same number of nodes, edges and degree of distribution as the elicited brain networks. The procedure can be described by the following steps: a pair of edges—(i_1, j_1) and (i_2, j_2)—were first randomly selected, where node i_1 is connected to node j_1, and node i_2 is connected to node j_2. If there were no edges between the two nodes, we added two new edges to replace the original two edges. This procedure is then repeated 2× the number of edges in the reference brain network to assure randomized organization.

2.6.4 | Degree of distribution fits

To determine whether the WM functional connectome included hub regions, three possible forms of the degree distribution $P(k)$ (Achard et al., 2006) were fitted to the WM functional connectome: a power law, $P(k) \sim k^{-\alpha}$; an exponential, $P(k) \sim e^{-\alpha k}$; and an exponentially truncated power law, $P(k) \sim k^{\alpha-1}e^{k/kc}$. To quantify the strength of each fit, goodness-of-fit was compared using Akaike's information criterion (AIC).

2.6.5 | Topological properties of the WM functional connectome

To validate the nonrandom topologies of the WM functional connectome, we compared the topological properties (E_{glob} and E_{loc}) between WM and random networks using a Wilcoxon signed-rank test. And we compared σ against 1 using a one-sample t test (Humphries, Gurney, & Prescott, 2006; Liao et al., 2011). Considering σ was the ratio of γ/λ, and that the same degree of distribution was found between WM and random networks, we did not compare the S, γ, and λ values between WM and random networks. The comparisons were first conducted for each sparsity values (0.17–0.42, interval = 0.01). We then calculated the area under curve (AUC) for E_{glob}, E_{loc} and σ using a range of sparsities from 0.17 to 0.42 for each subject. This AUC provides a summarized scalar for topological properties independent of single threshold selection, as any single threshold admits that the topological properties would be uniquely dependent on the precise threshold (Achard & Bullmore, 2007). The integrated AUC of topological properties has been used in previous brain network studies, and is sensitive to topological comparison (Ji et al., 2017; Liao et al., 2018).

2.6.6 | Correlation between topological properties and intelligence

We investigated the relationship between the topological properties (E_{glob}, E_{loc}, and σ) in the WM functional connectome, as well as fluid intelligence derived from the Combined Raven's Test (Sun et al., 2019) using Pearson's correlation coefficient. This test was used as a psychometric index of individual intelligence. We performed this correlational analysis on 402 out of 488 subjects who performed this behavioral test.

2.6.7 | Modular organization

To examine the modular organization of the WM functional connectome, we applied Newman's measure of modularity (Q) (Newman, 2006). A module in the network can be defined as a subdivision that has more connections within the module than outside the module.

2.6.8 | Test–retest analysis

To evaluate the reliability of global topological properties in the WM functional connectome, we applied a test–retest analysis. We created a group-level mask for subjects who took part in both studies, for whom both Time 1 and Time 2 data were available. We subdivided this group-level mask into 128 random ROIs. To minimize (scale) the effects of random networks, we used normalized E_{glob}, normalized E_{loc}, and σ values to process the test–retest analysis. Normalized E_{glob} was computed by the ratio of the E_{glob} of WM networks to the E_{glob} of comparable random networks, as well as normalized E_{loc}. We then calculated the topological properties (normalized E_{glob}, normalized E_{loc}, and σ) over a common range of sparsities range from 0.17 to 0.43 (interval = 0.01) across Time 1 and Time 2.

We evaluated the test–retest reliability of global topological properties (Andellini, Cannata, Gazzellini, Bernardi, & Napolitano, 2015; Wang et al., 2017) using the intraclass correlation coefficient (ICC). More specifically, a one-way ANOVA was used to evaluate the results of both scans in order to calculate the between-subject mean square (MS_b) and within-subject mean square (MS_w). ICC values were then calculated as follows:

$$\mathrm{ICC} = \frac{MS_b - MS_w}{MS_b + (d-1)MS_w}$$

where d is the number of observations per subject (here d = 2); MS_b is the between-subjects mean square; MS_w is the within-subjects mean square. We calculated the ICC values of topological properties for each specific sparsity. We classified ICC values into five levels according to the following criteria (Landis & Koch, 1977): excellent (ICC > 0.8), high (0.79 > ICC > 0.6), moderate (0.59 > ICC > 0.4), fair (0.39 > ICC > 0.2), and poor (ICC < 0.2).

2.7 | Comparison of topological properties between WM and GM functional connectomes

Using an identical method as used for WM, we constructed the functional connectome (128 × 128 correlation matrices) of GM. The GM group parcellation (GM.nii) used in the current study is attached as Supporting Information Data S1. Furthermore, we compared topological properties of the functional connectome between WM and GM.

For the GM functional connectome, the AUC of each topological property (S, E_{glob}, E_{loc}, γ, λ, and σ) was calculated using a range of sparsities from 0.11 to 0.48 (interval = 0.01) for each subject, separately. To compare the topological properties between WM and GM functional connectomes, a Wilcoxon signed-rank test was conducted for each sparsity value (range from 0.17 to 0.42, interval = 0.01), followed by a calculation of the integrated AUC of each topological property within a common range of sparsities from 0.17 to 0.42 (interval = 0.01).

2.8 | Validation analyses

We performed validation analysis in order to estimate the influence of head motion on the topological properties of the WM functional connectome. We also performed several additional analyses including global signal regression, without CSF regression, spatial (Euclidean) distance, and the node parcellation scheme, described in detail below. Moreover, considering that any interference would influence both WM and GM functional connectomes, we performed additional analyses comparing measured between WM and GM, such as the spatial (Euclidean) distance effect, global signal effect, and hemodynamic response function (HRF) effect.

1. Head motion effect: to validate whether the topological properties in the WM functional connectome were sensitive to head motion, we performed a Pearson's correlation analysis between mean FD and the AUC values of the topological properties.
2. Euclidean distance effect: as the observed WM nodes were all spatially very close to each other, this could lead to an overestimation of the clustering of the WM functional connectome. To exclude Euclidean distance effects for topological properties of the WM functional connectome, we regressed a Euclidean distance matrix from the WM functional connectivity matrices (Goni et al., 2014). The Euclidean distance D (in mm) was calculated by the 2-norm ($\|.\|_2$) of any pair of nodal centroids in the MNI stereotactic space (Misic et al., 2014; Salvador et al., 2005). The topological properties were then recalculated in these regressed matrices. In addition, we re-evaluated the modular organization of the WM functional connectome.

We then performed a comparison of topological properties between the WM and GM functional connectomes after regressing out the Euclidean distance matrix from both WM and GM functional connectivity matrices.

3. Global signal effect: we regressed out global brain signals (including WM, GM, and CSF tissues) during WM and GM functional data processing and maintained all other processes to validate the effect of global signals on our findings.

   After global signal regression, we compared topological properties between WM and GM functional connectomes, as well as between the WM functional connectome and random networks. In addition, we re-evaluated the topological properties (E_{glob}, E_{loc}, and σ) from the test–retest scans.

4. Node parcellation effect: we applied WM bundle masks using the JHU ICBM-DTI-81 WM atlas, as has been previously used (Ding et al., 2018; Wu et al., 2019) to validate the effects of node parcellation effect on topological property comparisons between the WM functional connectome and random networks. This WM atlas included 48 bundle regions (nodes).
5. CSF signal effect: to further explore the effects of CSF signals, we did not further regress out the brain CSF signals during preprocessing, maintaining all other processes intact. We validated the effect of CSF on topological property comparisons between the WM functional connectome and random networks.
6. HRF effect: there is expected to be a delay in BOLD-fMRI response between WM and GM signals (Li, Newton, Anderson, Ding, & Gore, 2019), which may affect the comparison of topological properties between WM and GM functional connectomes. To minimize any HRF delay effect, we used a blind-deconvolution technique for BOLD-fMRI signals to eliminate confounders, based on temporal precedence (https://github.com/compneuro-da/rsHRF) (Wu et al., 2013). During the resting state, BOLD-fMRI data were obtained by inspecting the discrete events that resulted in relatively large amplitude BOLD signal peaks, usually called spontaneous BOLD "events" (Liu & Duyn, 2013; Wu & Marinazzo, 2016). These events can then be used to retrieve the region-specific HRF at rest. In the present analysis, BOLD "events" were defined as the amplitude of time points exceeding 1 × SD of the time series surrounding a local peak (Liu & Duyn, 2013; Wu & Marinazzo, 2016). Then, we used the corresponding HRF in a deconvolution model to obtain the deconvolved BOLD-fMRI signal. Finally, we constructed both the WM and GM functional connectomes using this deconvolved BOLD-fMRI signal.
7. Thresholding methods effect: Sparsity thresholding has been suggested to influence the underlying graph metrics. As a form of validation analysis, we performed an additional thresholding method—calculation of the correlation coefficient (r) (Liao et al., 2010, 2011)—to explore the topological properties (E_{glob}, E_{loc}, and σ) of the WM functional connectome against random networks.

3 | RESULTS

3.1 | Network visualizations

Figure 2a displays the averaged WM functional connectivity matrix (sparsity = 0.15) across all subjects at Time 1. The matrix values represent the connection strength between each two paired nodes.

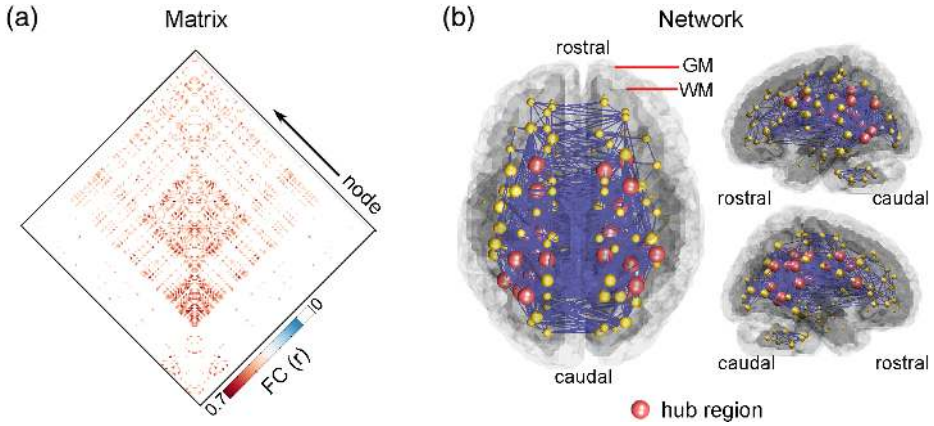

FIGURE 2 Correlation matrix and functional connectome visualization. (a) A correlation matrix of the 128 ROIs with sparsity = 0.15 was constructed by averaging the correlation matrices across 488 subjects who had participated in scanning at Time 1. (b) An anatomical projection of the 128-ROIs of the WM functional connectome (sparsity = 0.15). Each node depicted at its appropriate anatomical position (Table S2). Blue edges represent links between nodes. Node colors indicate the hub region: Red indicates a hub region, and yellow indicates an anatomical position that is not a hub region. ROI, region-of-interest; WM, white-matter [Color figure can be viewed at wileyonlinelibrary.com]

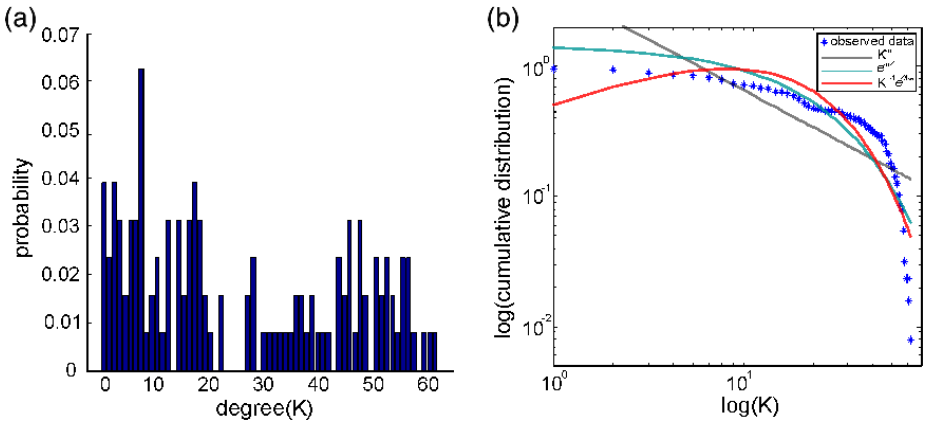

FIGURE 3 The degree distributions of the 128-ROIs of the WM functional connectome. (a) Regional degree distribution and the cumulative probability of degree. (b) The blue asterisks represent the observed data. The red line denotes the best-fitting exponentially truncated power law. The cyan line, and gray line indicate the fit of an exponential distribution, and a power law distribution, respectively see Table S1 for parameter values and goodness-of-fit. ROI, region of interest; WM, white-matter [Color figure can be viewed at wileyonlinelibrary.com]

Figure 2b illustrates the spatial patterns of this functional connectome consisting of the network diagram of nodes and edges. Brain hubs were defined as the ROIs with a relatively high node degree (>mean + *SD*; Figure 2b). These hubs exhibit a large number of connections (Achard et al., 2006), and play an important integrative role in the functional connectome. In this study, hubs were primarily distributed in the posterior thalamic radiation, superior corona radiation, and superior longitudinal fasciculus. Multimodal brain networks exhibited a power law degree distribution.

3.2 | Degree distribution

Figure 3a shows the regional degree distribution and the cumulative probability of degree of WM functional connectome (sparsity = 0.15). In addition, the WM functional connectome showed a best-fitting exponentially truncated power law distribution, rather than a simple power law distribution or exponential distribution (Figure 3b), indicating the existence of highly connected hubs. See Table S1 for parameter values and goodness-of-fit.

3.3 | Topological properties of the WM functional connectome

We compared E_{glob} and E_{loc} attributes between the WM and random networks, as well as small-worldness (σ) against 1 under the range of sparsities (0.17–0.42) (Figure 4). The WM functional connectome exhibited higher σ than 1 across the entire range of sparsities, as well as an AUC value (one-sample t test, $t = 21.63$, $p < .05$, Bonferroni correction). Compared to random networks, the WM functional connectome showed decreased E_{glob} (Wilcoxon signed-rank test, $p < .05$, Bonferroni correction) and increased E_{loc} (Wilcoxon signed-rank test, $p < .05$, Bonferroni correction) not only at each sparsity value but also compared to the AUC value.

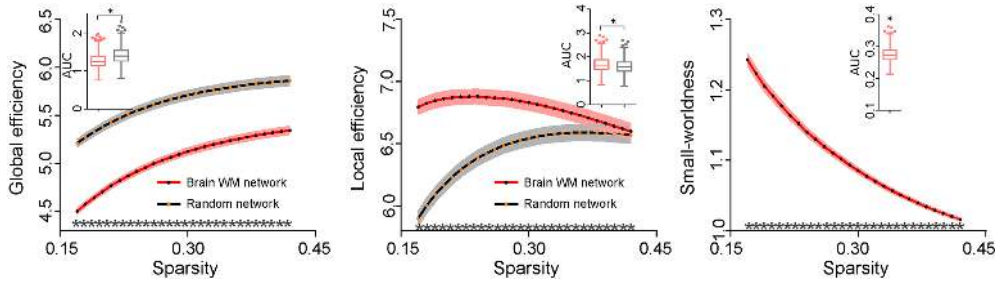

FIGURE 4 Topological properties of the WM functional connectome. E_{glob} and E_{loc} (*y*-axis) as a function of sparsity (*x*-axis) of the WM functional connectome and a random graph (left, and middle planes). The small-worldness (σ, *y*-axis) is shown as a function of sparsity (*x*-axis) of the WM functional connectome (middle plane). For all networks, the WM functional connectome (the black dots and red lines) showed decreased E_{glob} and increased E_{loc} compared to random network (the orange dots and black lines). The WM functional connectome also showed weak small-worldness, that is, σ is higher than 1 (one sample *t* test, $p < .05$, Bonferroni correction). Similarly, the WM functional connectome showed decreased AUC values of E_{glob} and increased AUC values of E_{loc} against a random graph and higher AUC values of small-worldness (σ) against 0.25 (the AUC value of 1 across all sparsities). Gray asterisks indicate that there are significant differences (Wilcoxon signed-rank test, $p < .05$, Bonferroni correction) in topological properties between the WM functional connectome and random networks for specific sparsity and AUC values. AUC, area under curve; E_{glob}, global efficiency; E_{loc}, local efficiency; WM, white-matter [Color figure can be viewed at wileyonlinelibrary.com]

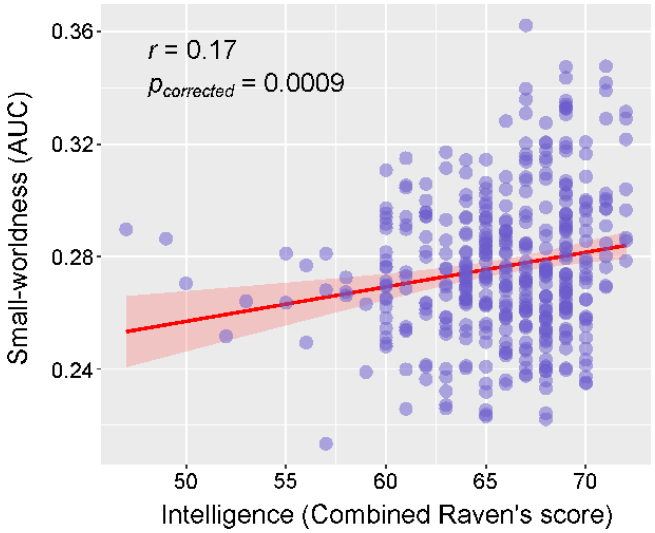

FIGURE 5 Correlation between AUC values of small-worldness and individuals' intelligence. Filled blue circles represent subjects ($n = 402$) who performed a behavioral test. Red line and light red interval represent the best-fit and 95% confidence of interval of Pearson's correlation, respectively. $p_{corrected}$ means the *p* value survived after Bonferroni correction. AUC, area under curve [Color figure can be viewed at wileyonlinelibrary.com]

Furthermore, we found that the AUC values of σ positively correlated with fluid intelligence ($r = .17$, $p_{corrected} = .0009$, Bonferroni correction for three times planned comparisons; Figure 5), indicating a role for WM function in cognitive ability. There was no statistically significant correlation found between the other topological properties (E_{glob}, and E_{loc}) and fluid intelligence.

3.4 | Modularity of the WM functional connectome

Using Newman's modularity algorithm, we found that the WM functional connectome was separated into four modules (Figure 6). Brain regions with these modules were found to be symmetrical across the two cerebral hemispheres, and were located in specific anatomical bundles, suggesting a nonrandom spatial distribution. In addition, the modules exhibited dense connectivity between each node (colored lines in Figure 6), and sparser connectivity between nodes of different modules (gray lines in Figure 6). Module I included 40 brain regions that were mainly located in the bilateral anterior/superior corona radiata, and the genu/body of the corpus callosum. Module II included 41 brain regions, such as the posterior corona radiata, superior longitudinal fasciculus, and splenium of the corpus callosum. Module III included 21 brain regions located mostly within the optic radiation. Module IV included 26 brain regions such as the cerebellar peduncle and the anterior/posterior limb of the internal capsule. The anatomical location (MNI coordinates) of each node, nodal degree, and designated module are list in Table S2.

3.5 | Global topological properties reliability

We quantified the long-term test–retest reliability of global topological properties (including normalized E_{glob}, normalized E_{loc}, and σ) of the WM functional network using ICC scores. We obtained the ICC values of topological properties across the entire range of sparsities from 0.17 to 0.43 (Figure 7). The ICC values of normalized E_{glob} were moderate, whereas the ICC values of normalized E_{loc}, and σ were fair relative to sparsity.

3.6 | Comparisons between WM and GM functional connectomes

We compared global topological properties including *S*, E_{glob}, E_{loc}, γ, λ, and σ between the WM and GM functional connectomes under the common range of sparsities (0.17–0.42) (Figure 8). We found that the WM functional connectome exhibited decreased E_{glob}, γ, λ, and σ, while there was an increase in *S* and E_{loc} compared to the GM

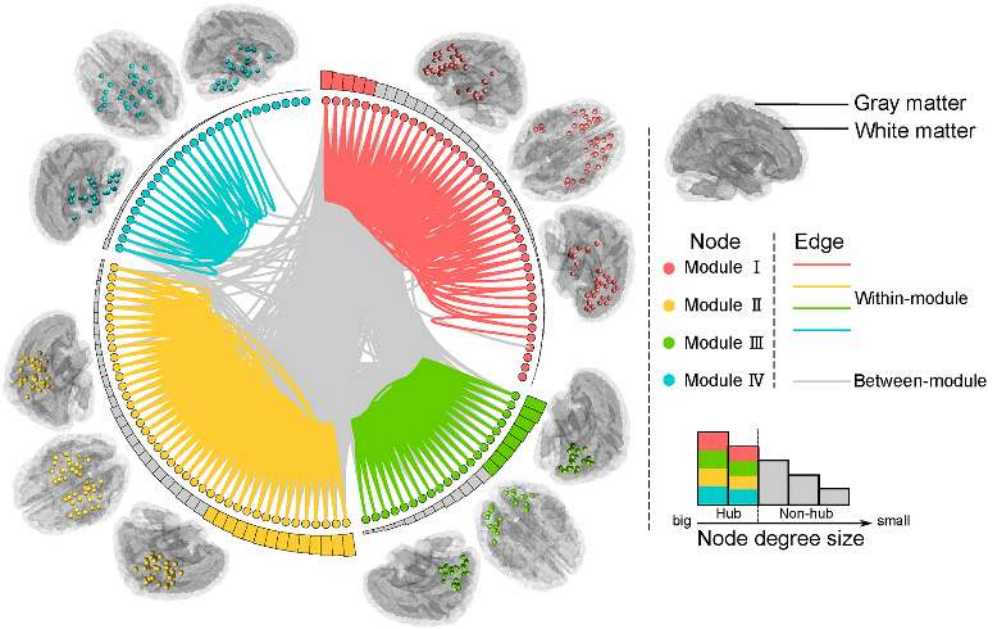

FIGURE 6 Modularity of WM functional connectome. The 128-ROIs WM functional connectome identified four link-based modules, which are shown in a connectogram using DynamicBC (V2.2, www.restfmri.net/forum/DynamicBC). Lines crossing the diameter of the circle represent functional connections between ROIs (circles). The colored and gray lines represent within-module and between-module connections, respectively. The outer bars are sorted by degree, with colored bars indicating hub regions (k > mean + SD) (Table S2). Other locations are nonhub regions. The outer-most brain graphs show each module individually, with nodes representing functional subregions within the module. ROI, region of interest; SD, standard deviation; WM, white-matter [Color figure can be viewed at wileyonlinelibrary.com]

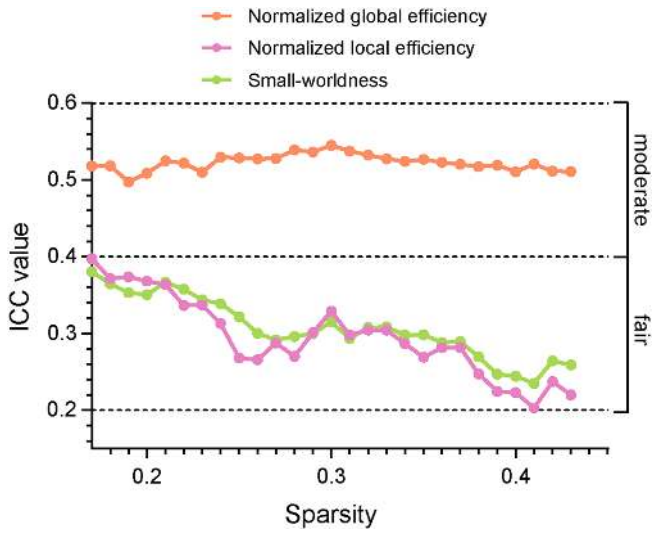

FIGURE 7 The reliability of global topological properties in the WM functional connectome. ICC values represent the reliability of global topological properties. To minimize random network effects, the ICC values of normalized E_{glob}, normalized E_{loc} and small-worldness (σ) were computed. ICC values (y-axis) of each global topological property (different colored lines) are plotted as a function of network sparsity (x-axis). The ICC values of normalized E_{glob} were at moderate level and ICC values of normalized E_{loc} and small-worldness (σ) were at a fair level. E_{glob}, global efficiency; E_{loc}, local efficiency; ICC, intraclass correlation coefficient; WM, white-matter [Color figure can be viewed at wileyonlinelibrary.com]

functional connectome (Wilcoxon signed-rank test p < .05, Bonferroni correction for six times planned comparisons) under specific sparsities and AUC values. Results suggested that the WM functional connectome shifts towards randomization with a loss of segregation and a preference for global integration.

3.7 | Validation results

1. There were no significant correlations between head motion parameters (mean FD) and the AUC of the topological properties of the WM functional network (all p > .05; Table S3). This finding suggests that the topological properties of the WM functional network cannot be explained by head motion.
2. Firstly, we found that shorter spatial distances (Euclidean distance) between the centroids of nodes were correlated with higher functional connectivity strength in the WM functional connectome (Figure S1). The relationship between Euclidean distance and functional connectivity in WM was most likely nonlinear, which can be approximated by an inverse square law: $z \sim 1/D^2$ (Salvador et al., 2005).

After regressing out spatial distance from functional connectivity matrices, we found that the global topological properties (E_{glob}, E_{loc}, and σ) showed similar tendencies with our original results. The WM functional connectome also showed decreased E_{glob} and increased E_{loc} compared to random networks, while the WM functional connectome exhibited higher σ than 1 under parts of specific sparsity and AUC

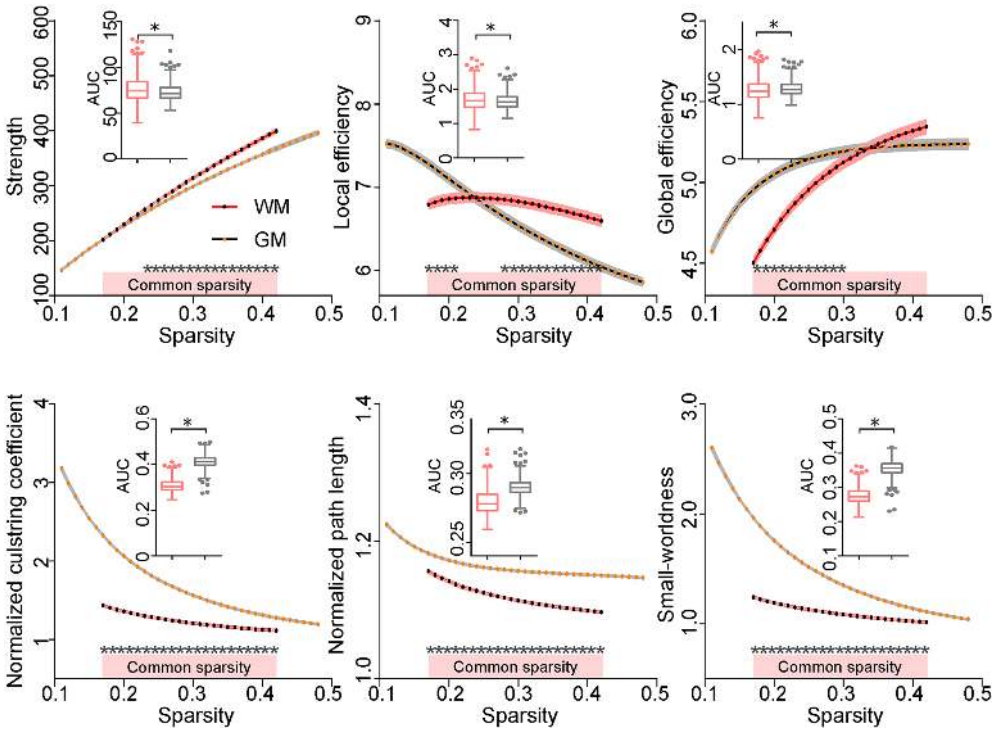

FIGURE 8 Comparison of global topological properties between the WM and GM functional connectomes. The global topological properties (*y*-axis) are plotted as a function of network sparsity (*x*-axis). The black dots and red lines represent the WM functional connectome. The orange dots and black lines represent the GM functional connectome. The inset boxplot represents the AUC of topological properties under a common range of sparsities (0.17–0.42) in WM and GM functional connectomes. Gray asterisks indicate significant differences (Wilcoxon signed-rank test, $p < .05$, Bonferroni correction) in topological properties between WM and GM functional connectomes at specific sparsity values. *$p < .05$, Bonferroni correction. AUC, area under the curve; GM, gray-matter; WM, white-matter [Color figure can be viewed at wileyonlinelibrary.com]

value (Figure S2). In addition, the WM functional connectome was separated into five modules (Figure S3). These findings suggest that spatial distance has no significant effect on topological properties (E_{glob}, E_{loc}, and σ), as well as the presence of a nonrandom modular organization of the WM functional connectome.

Moreover, we found a consistent difference in global topological properties (S, E_{glob}, γ, λ, and σ) between WM and GM functional connectomes (Figure S4). These findings suggest that the topological properties of the WM functional network cannot be totally accounted for by the spatial distance of nodes.

3. Similarly, after regressing out global signal, we found that the global topological properties (E_{glob}, E_{loc}, and σ) showed similar tendencies as the observed properties without global signal regression (Figure S5). Also, the ICC values of normalized E_{glob} showed a moderate level, while the ICC values of normalized E_{loc}, and σ showed a fair level; the same as global signal regression (Figure S6). In addition, we also found a consistent difference in global topological properties (S, E_{glob}, E_{loc}, γ and σ), between the WM and GM functional connectomes (Figure S7).
4. We used WM bundle nodes, as utilized in a previous study by Ding et al. (2018), to investigate the WM functional connectome. This bundle based functional connectome also exhibited similar topological properties tendencies to our predefined nodes. The WM functional connectome showed decreased E_{glob} and increased E_{loc} and higher σ against 1 in parts of sparsities. The topological properties are shown in Figure S8.
5. After CSF signal nonregression, we found that the topological properties (E_{glob}, E_{loc}, and σ) showed similar tendencies to our main results in which the CSF signal was regressed out (Figure S9).
6. After considering the HRF between WM and GM nodes, we found that the WM functional connectome also exhibited decreased E_{glob}, γ, λ, and σ compared to the GM functional connectome. However, the comparisons of S and E_{loc} differed from the original results that did not exclude HRF effects (Figure S10).
7. After performing an additional thresholding method—correlation coefficient (r), we found that the WM functional connectome showed weak σ. Similarly, the WM functional connectome also exhibited decreased E_{glob} and increased E_{loc} compared to the random networks (Figure S11).

4 | DISCUSSION

The functional role of WM BOLD-fMRI signals is a longstanding controversy. The first debate relates to the way in which WM, relative to GM, contains lower cerebral blood flow and volume. The cerebral blood flow and volumes are the basis of the BOLD signal in neural

activity (Preibisch & Haase, 2001; Rostrup et al., 2000). Another debate centers on how BOLD signals are associated with local field action potentials in GM, while not reflecting action potentials in WM (Gawryluk, Mazerolle, & D'Arcy, 2014).

However, in comparison to GM, and regardless of large discrepancies in respect to the physiological factors observed between GM and WM, WM maintains a higher ratio of glial cells to neurons (Azevedo et al., 2009), while showing an approximately equal oxygen extraction fraction (Raichle et al., 2001). In addition, in task-related fMRI studies, external stimuli can reliably induce the WM hemodynamic with a profile similar to that observed in GM, though with a smaller peak amplitude (Huang et al., 2018). Resting-state fMRI studies have recently shown that WM and GM exhibit similar low frequency signal powers (Ding et al., 2013, 2016; Ji, Liao, Chen, Zhang, & Wang, 2017). Further, BOLD-fMRI signals of intrinsic functional networks in WM were highly correlated with those observed in GM, suggesting that WM manifests an intrinsic functional organization (Ding et al., 2018; Jiang et al., 2019; Peer et al., 2017). Taken together, these findings suggest that there are no fundamental barriers or direct sources of evidence against the possibility of detecting neural activities of BOLD-fMRI in WM (Gawryluk, Mazerolle, & D'Arcy, 2014). To date, many psychiatric and neurological disorders are characterized by WM functional abnormalities (Ji et al., 2019; Jiang et al., 2019; Jiang et al., 2019; Wang et al., 2019). It is therefore important to explore WM functional networks to allow for fMRI-based investigations of WM brain disorders, such as multiple sclerosis (He et al., 2009), and WM dementia (Filley, 2012), which may allow further insight into our understanding of the pathological mechanisms of different neurological diseases. The current study extends the findings of WM activity/connectivity to large-scale understanding of WM network architecture and mechanisms, thus offering a new approach to elucidating our understanding of brain functioning.

Understanding how connectivity varies across nodes is a fundamental step in network analysis (Sporns, 2012). Furthermore, the degree distribution allows us to investigate whether hubs exist in a network, and to obtain greater insight into the potential brain functioning of network hubs. We found that the degree distribution of the WM functional connectome obeyed an exponentially truncated power law, rather than a power law or an exponential distribution. This finding is consistent with previous human GM functional connectome and WM anatomical connectome research (Achard et al., 2006). This exponentially truncated power law degree distribution implies that WM functional connectomes are also organized within some core regions, though they prevent the emergence of hubs with a very large number of links (Bullmore & Sporns, 2009). More specifically, the current degree distribution often features a long tail that tends towards high degrees, termed hub regions. This heterogeneous distribution implies that different brain regions (i.e., nodes) serve distinct topological roles in the network (Hagmann et al., 2008; He et al., 2009). In this study, we identified putative hub regions located mainly in the posterior thalamic radiation, superior corona radiata, and superior longitudinal fasciculus. We did not directly compare hub regions with the findings of previous research, where nodes were defined in GM. However, we present evidence for hub regions, such as the thalamus in GM (van den Heuvel, Mandl, Stam, Kahn, & Hulshoff Pol, 2010), as the thalamic radiation encompasses the fibers between the thalamus and the cerebral cortex. In light of such evidence, it seems possible that this hub region plays a key role in the integration of information involving such complex processes.

Optimized small-worldness may be a hallmark of brain connectomes (Bassett & Bullmore, 2017). Therefore, this property should also be observed for the WM functional connectome. Although the present measure of σ was found to be statistically higher against 1—the numerically value was close to 1, suggesting there may be a weak small-worldness organization. In addition, there is evidence indicating that BOLD-fMRI signals represent nonrandom noise and nonartifacts (Ji, Liao, Chen, Zhang, & Wang, 2017; Marussich et al., 2017). To test for robustness, we re-calculated small-worldness when performing global signal regression, Euclidean distance regression, CSF signal nonregression, and differential node parcellations (i.e., WM fiber bundle-based nodes). We found that small-worldness was statistically higher than 1 in each condition abovementioned. Furthermore, there were no significant correlations between head motion parameters (mean FD) and small-worldness. Moreover, the reliability of the current long-term global topological properties was found to be fair to moderate, similar to that previously reported for the GM functional connectome findings. These results underscore the reliability of our findings. Finally, the small-worldness positively associated with intelligence, suggesting a more optimized efficient parallel information transfer system in the brain. Taken together, these results indicate that small-worldness is a fundamental property of anatomical, functional, and even WM functional connectomes, indicating that these networks can facilitate synchronization and information propagation.

The WM functional connectome showed a shift towards randomization (i.e., a loss of segregation, and a favoring global integration) compared to GM. Measures of segregation indicate specialized processing that occurs within densely interconnected brain regions (Wig, 2017). A less segregated or specialized topological organization may be beneficial for network function (Chan, Park, Savalia, Petersen, & Wig, 2014). Measures of integration estimate the ability to combine specialized information among distributed brain regions. A preference for global integration may promote the efficiency of global communication, and integrate distributed information. Taken together, less segregation and a preference for integration results in network randomization. This subtle randomization is consistent with previous findings, which suggest that fMRI network randomization is a marker of a genetic or shared environmental risk for a brain disorder. Randomization is also consistent with the degree distribution being fat-tailed. Thus, it can be predicted that the WM functional connectome is topologically more random than that observed in GM.

The WM functional connectome also showed increased network strength relative to the GM functional connectome. This finding may be due to the fact that our ROIs were constrained by WM fiber bundles, thus enabling ROIs within one fiber bundle to participate in more direct connections (Honey et al., 2009). This is supported by the observation that visual stimulation induces BOLD activation in

specific WM bundles (Ding et al., 2018; Ji, Liao, Chen, Zhang, & Wang, 2017). Furthermore, the factors that impact the results of comparisons between WM and GM functional connectomes are diverse, such as spatial distance, global signals, and fMRI response in ROIs. These factors should be accounted for in future seeking to make comparisons between WM and GM functional connectomes. In this context, the topological differences we describe are empirically novel, although conceptually unsurprising, particularly in terms of elucidating WM functional networks in a pathophysiological state (Ji et al., 2019).

Not all small-word networks are modular (Sporns, 2012). However, consistent with multiple human brain networks (Hagmann et al., 2008; He et al., 2009), we found that the WM functional connectome also exhibited a nonrandom modular topology. This modular organization would be energetically favorable, in that it conserves wiring cost, and would also create specialized information (Sporns & Betzel, 2016). Not only would spatially compact, modules conserve wiring costs, it would lead to functional constraints, supporting the idea that brain connectome topology is shaped by a trade-off between spatial and functional considerations (Bullmore & Sporns, 2012). In contrast, the persistence of modular organization, cross-linked by long-distance ties, is crucial for creating specialized information (Gallos, Makse, & Sigman, 2012). Our results support the hypothesis that each module executes a discrete function. More specifically, Module I is primarily specialized for a high-level cognitive system, supporting both bottom-up and top-down stimulus-processing (Westerhausen & Hugdahl, 2008). Modules II, III, and IV are primarily specialized for a low-level perceptive system (Westerhausen & Hugdahl, 2008). These results suggest discrete cognitive functions in the WM network, thereby offering new insight into our understanding of functional segregation and the integration of brain networks.

4.1 | Methodological considerations

In the current study, we first strictly controlled the mixed WM and GM BOLD-fMRI signals (Ji, Liao, Chen, Zhang, & Wang, 2017) in order to minimize the contribution of partial volume effects from adjacent GM to WM BOLD fMRI signals (Gawryluk, Mazerolle, & D'Arcy, 2014). Additionally, we employed several parallel data analysis methods to provide a rich pool of information as well as further cross-validation of our findings. Nevertheless, these findings also produced parts of inconsistent results when comparing topological properties between WM and GM functional connectomes. Such divergence might be driven by closer WM spatial distances than found in GM and with or without global signal regression, as well as differences in the fMRI responses between WM and GM. Secondly, we considered five influence factors, including the effects of spatial distance, global signals, CSF signals, node parcellation, and alternative thresholding methods (correlation-based) to construct the WM functional connectome. Primarily, we found that the WM functional connectome showed weak small-worldness and similar tendencies even after accounting for these factors. In addition, the comparisons of topological properties are not consistent across all sparsities in differential factors, thus, we made our conclusion according to the AUC results.

4.2 | Limitations

One limitation of the methods used in this study entails the multiple methodological choices for constructing the brain's connectome. The data preprocessing and analytic strategies may influence the network pattern. We have addressed these issues by testing the key findings to ensure that they are robust with respect to contemporary processing strategies for head motion correction (Power et al., 2012) and for reasonable variation in the other analytic steps, including choice of mask parcellation and brain global signal regression. Second, although the significant differences in our results (WM vs. random, WM vs. GM), the effect size was relatively small. Finally, as the present shared data were assembled without physiological recordings, future studies may wish to record and consider physiological data to validate the effects of WM function.

In conclusion, we demonstrate that the brain's WM functional connectome architecture includes small-world topology, high-degree hubs, and a nonrandom modular organization. The global topological properties were reliable in the long-term and were replicable across the node parcellation strategy, global signal regression, spatial distance regression, and head motion effects. This suggests that the WM functional connectome cannot be attributed simply to noise. We also found that the WM functional connectome has a tendency towards randomization compared to the GM functional connectome, adding a new dimension to investigate brain networks. The current findings offer evidence for a previously unappreciated WM connectome, and presents a novel approach to elucidating our understanding of WM functional information in both healthy individuals and in cases of clinical disease.

ACKNOWLEDGMENTS

We are grateful to all the participants in this study. We thank International Science Editing (http://www.internationalscienceediting.com) for editing this manuscript. This work was supported by the National Natural Science Foundation of China (61871077, 61533006, U1808204, 81771919, and 61673089), China Postdoctoral Science Foundation (2013M532229), Sichuan Science and Technology Program (2018TJPT0016), and the “111” Project (B12027).

CONFLICT OF INTERESTS

The authors declare no conflict of interest.

DATA ACCESSIBILITY

The data that support the findings of this study are available in the International Data-sharing Initiative at http://fcon_1000.projects.nitrc.org/, related to Southwest University Longitudinal Imaging Multimodal (SLIM).

REFERENCES

Achard, S., & Bullmore, E. (2007). Efficiency and cost of economical brain functional networks. *PLoS Computational Biology*, *3*, e17.

Achard, S., Salvador, R., Whitcher, B., Suckling, J., & Bullmore, E. (2006). A resilient, low-frequency, small-world human brain functional network with highly connected association cortical hubs. *The Journal of Neuroscience*, *26*, 63–72.

Andellini, M., Cannata, V., Gazzellini, S., Bernardi, B., & Napolitano, A. (2015). Test–retest reliability of graph metrics of resting state MRI functional brain networks: A review. *Journal of Neuroscience Methods*, *253*, 183–192.

Ashburner, J. (2007). A fast diffeomorphic image registration algorithm. *NeuroImage*, *38*, 95–113.

Ashburner, J., & Friston, K. J. (2009). Computing average shaped tissue probability templates. *NeuroImage*, *45*, 333–341.

Avena-Koenigsberger, A., Misic, B., & Sporns, O. (2017). Communication dynamics in complex brain networks. *Nature Reviews. Neuroscience*, *19*, 17–33.

Azevedo, F. A., Carvalho, L. R., Grinberg, L. T., Farfel, J. M., Ferretti, R. E., Leite, R. E., … Herculano-Houzel, S. (2009). Equal numbers of neuronal and nonneuronal cells make the human brain an isometrically scaled-up primate brain. *The Journal of Comparative Neurology*, *513*, 532–541.

Bassett, D. S., & Bullmore, E. T. (2017). Small-world brain networks revisited. *The Neuroscientist*, *23*, 499–516.

Biswal, B., Yetkin, F. Z., Haughton, V. M., & Hyde, J. S. (1995). Functional connectivity in the motor cortex of resting human brain using echo-planar MRI. *Magnetic Resonance in Medicine*, *34*, 537–541.

Biswal, B. B., Mennes, M., Zuo, X. N., Gohel, S., Kelly, C., Smith, S. M., … Milham, M. P. (2010). Toward discovery science of human brain function. *Proceedings of the National Academy of Sciences of the United States of America*, *107*, 4734–4739.

Bullmore, E., & Sporns, O. (2009). Complex brain networks: Graph theoretical analysis of structural and functional systems. *Nature Reviews. Neuroscience*, *10*, 186–198.

Bullmore, E., & Sporns, O. (2012). The economy of brain network organization. *Nature Reviews. Neuroscience*, *13*, 336–349.

Bullmore, E. T., & Bassett, D. S. (2011). Brain graphs: Graphical models of the human brain connectome. *Annual Review of Clinical Psychology*, *7*, 113–140.

Chan, M. Y., Park, D. C., Savalia, N. K., Petersen, S. E., & Wig, G. S. (2014). Decreased segregation of brain systems across the healthy adult lifespan. *Proceedings of the National Academy of Sciences of the United States of America*, *111*, E4997–E5006.

Courtemanche, M. J., Sparrey, C. J., Song, X., MacKay, A., & D'Arcy, R. C. N. (2018). Detecting white matter activity using conventional 3 tesla fMRI: An evaluation of standard field strength and hemodynamic response function. *NeuroImage*, *169*, 145–150.

D'Arcy, R. C., Hamilton, A., Jarmasz, M., Sullivan, S., & Stroink, G. (2006). Exploratory data analysis reveals visuovisual interhemispheric transfer in functional magnetic resonance imaging. *Magnetic Resonance in Medicine*, *55*, 952–958.

Ding, Z., Huang, Y., Bailey, S. K., Gao, Y., Cutting, L. E., Rogers, B. P., … Gore, J. C. (2018). Detection of synchronous brain activity in white matter tracts at rest and under functional loading. *Proceedings of the National Academy of Sciences of the United States of America*, *115*, 595–600.

Ding, Z., Newton, A. T., Xu, R., Anderson, A. W., Morgan, V. L., & Gore, J. C. (2013). Spatio-temporal correlation tensors reveal functional structure in human brain. *PLoS One*, *8*, e82107.

Ding, Z., Xu, R., Bailey, S. K., Wu, T. L., Morgan, V. L., Cutting, L. E., … Gore, J. C. (2016). Visualizing functional pathways in the human brain using correlation tensors and magnetic resonance imaging. *Magnetic Resonance Imaging*, *34*, 8–17.

Filley, C. M. (2012). White matter dementia. *Therapeutic Advances in Neurological Disorders*, *5*, 267–277.

Gallos, L. K., Makse, H. A., & Sigman, M. (2012). A small world of weak ties provides optimal global integration of self-similar modules in functional brain networks. *Proceedings of the National Academy of Sciences of the United States of America*, *109*, 2825–2830.

Garrison, K. A., Scheinost, D., Finn, E. S., Shen, X., & Constable, R. T. (2015). The (in)stability of functional brain network measures across thresholds. *NeuroImage*, *118*, 651–661.

Gawryluk, J. R., Mazerolle, E. L., Beyea, S. D., & D'Arcy, R. C. (2014). Functional MRI activation in white matter during the symbol digit modalities test. *Frontiers in Human Neuroscience*, *8*, 589.

Gawryluk, J. R., Mazerolle, E. L., Brewer, K. D., Beyea, S. D., & D'Arcy, R. C. (2011). Investigation of fMRI activation in the internal capsule. *BMC Neuroscience*, *12*, 56.

Gawryluk, J. R., Mazerolle, E. L., & D'Arcy, R. C. (2014). Does functional MRI detect activation in white matter? A review of emerging evidence, issues, and future directions. *Frontiers in Neuroscience*, *8*, 239.

Goni, J., van den Heuvel, M. P., Avena-Koenigsberger, A., Velez de Mendizabal, N., Betzel, R. F., Griffa, A., … Sporns, O. (2014). Resting-brain functional connectivity predicted by analytic measures of network communication. *Proceedings of the National Academy of Sciences of the United States of America*, *111*, 833–838.

Hagmann, P., Cammoun, L., Gigandet, X., Meuli, R., Honey, C. J., Wedeen, V. J., & Sporns, O. (2008). Mapping the structural core of human cerebral cortex. *PLoS Biology*, *6*, e159.

He, Y., Chen, Z. J., & Evans, A. C. (2007). Small-world anatomical networks in the human brain revealed by cortical thickness from MRI. *Cerebral Cortex*, *17*, 2407–2419.

He, Y., Dagher, A., Chen, Z., Charil, A., Zijdenbos, A., Worsley, K., & Evans, A. (2009). Impaired small-world efficiency in structural cortical networks in multiple sclerosis associated with white matter lesion load. *Brain*, *132*, 3366–3379.

He, Y., Wang, J., Wang, L., Chen, Z. J., Yan, C., Yang, H., … Evans, A. C. (2009). Uncovering intrinsic modular organization of spontaneous brain activity in humans. *PLoS One*, *4*, e5226.

Honey, C. J., Sporns, O., Cammoun, L., Gigandet, X., Thiran, J. P., Meuli, R., & Hagmann, P. (2009). Predicting human resting-state functional connectivity from structural connectivity. *Proceedings of the National Academy of Sciences of the United States of America*, *106*, 2035–2040.

Huang, Y., Bailey, S. K., Wang, P., Cutting, L. E., Gore, J. C., & Ding, Z. (2018). Voxel-wise detection of functional networks in white matter. *NeuroImage*, *183*, 544–552.

Humphries, M. D., Gurney, K., & Prescott, T. J. (2006). The brainstem reticular formation is a small-world, not scale-free, network. *Proceedings of the Biological Sciences*, *273*, 503–511.

Ji, G. J., Liao, W., Chen, F. F., Zhang, L., & Wang, K. (2017). Low-frequency blood oxygen level-dependent fluctuations in the brain white matter: More than just noise. *Scientific Bulletin*, *62*, 656–657.

Ji, G. J., Ren, C., Li, Y., Sun, J., Liu, T., Gao, Y., … Wang, K. (2019). Regional and network properties of white matter function in Parkinson's disease. *Human Brain Mapping*, *40*, 1253–1263.

Ji, G. J., Yu, Y., Miao, H. H., Wang, Z. J., Tang, Y. L., & Liao, W. (2017). Decreased network efficiency in benign epilepsy with centrotemporal spikes. *Radiology*, *283*, 186–194.

Jiang, Y., Luo, C., Li, X., Li, Y., Yang, H., Li, J., … Yao, D. (2019). White-matter functional networks changes in patients with schizophrenia. *NeuroImage*, *190*, 172–181.

Jiang, Y., Song, L., Li, X., Zhang, Y., Chen, Y., Jiang, S., … Luo, C. (2019). Dysfunctional white-matter networks in medicated and unmedicated benign epilepsy with centrotemporal spikes. *Human Brain Mapping*, *40*, 3113–3124.

Landis, J. R., & Koch, G. G. (1977). The measurement of observer agreement for categorical data. *Biometrics*, *33*, 159–174.

Latora, V., & Marchiori, M. (2001). Efficient behavior of small-world networks. *Physical Review Letters*, *87*, 198701.

Li, M., Newton, A. T., Anderson, A. W., Ding, Z., & Gore, J. C. (2019). Characterization of the hemodynamic response function in white matter tracts for event-related fMRI. *Nature Communications*, *10*, 1140.

Liao, W., Ding, J., Marinazzo, D., Xu, Q., Wang, Z., Yuan, C., … Chen, H. (2011). Small-world directed networks in the human brain: Multivariate Granger causality analysis of resting-state fMRI. *NeuroImage*, *54*, 2683–2694.

Liao, W., Li, J., Duan, X., Cui, Q., Chen, H., & Chen, H. (2018). Static and dynamic connectomics differentiate between depressed patients with and without suicidal ideation. *Human Brain Mapping*, *39*, 4105–4118.

Liao, W., Li, J., Ji, G. J., Wu, G. R., Long, Z., Xu, Q., … Chen, H. (2019). Endless fluctuations: Temporal dynamics of the amplitude of low frequency fluctuations. *IEEE Transactions on Medical Imaging*. https://doi.org/10.1109/TMI.2019.2904555

Liao, W., Zhang, Z., Pan, Z., Mantini, D., Ding, J., Duan, X., … Chen, H. (2010). Altered functional connectivity and small-world in mesial temporal lobe epilepsy. *PLoS One*, *5*, e8525.

Liu, W., Wei, D., Chen, Q., Yang, W., Meng, J., Wu, G., … Qiu, J. (2017). Longitudinal test–retest neuroimaging data from healthy young adults in Southwest China. *Scientific Data*, *4*, 170017.

Liu, X., & Duyn, J. H. (2013). Time-varying functional network information extracted from brief instances of spontaneous brain activity. *Proceedings of the National Academy of Sciences of the United States of America*, *110*, 4392–4397.

Makedonov, I., Chen, J. J., Masellis, M., & MacIntosh, B. J. (2016). Physiological fluctuations in white matter are increased in Alzheimer's disease and correlate with neuroimaging and cognitive biomarkers. *Neurobiology of Aging*, *37*, 12–18.

Marussich, L., Lu, K. H., Wen, H., & Liu, Z. (2017). Mapping white-matter functional organization at rest and during naturalistic visual perception. *NeuroImage*, *146*, 1128–1141.

Maslov, S., & Sneppen, K. (2002). Specificity and stability in topology of protein networks. *Science*, *296*, 910–913.

Misic, B., Fatima, Z., Askren, M. K., Buschkuehl, M., Churchill, N., Cimprich, B., … Berman, M. G. (2014). The functional connectivity landscape of the human brain. *PLoS One*, *9*, e111007.

Newman, M. E. (2006). Modularity and community structure in networks. *Proceedings of the National Academy of Sciences of the United States of America*, *103*, 8577–8582.

Peer, M., Nitzan, M., Bick, A. S., Levin, N., & Arzy, S. (2017). Evidence for functional networks within the human brain's white matter. *The Journal of Neuroscience*, *37*, 6394–6407.

Power, J. D., Barnes, K. A., Snyder, A. Z., Schlaggar, B. L., & Petersen, S. E. (2012). Spurious but systematic correlations in functional connectivity MRI networks arise from subject motion. *NeuroImage*, *59*, 2142–2154.

Preibisch, C., & Haase, A. (2001). Perfusion imaging using spin-labeling methods: Contrast-to-noise comparison in functional MRI applications. *Magnetic Resonance in Medicine*, *46*, 172–182.

Raichle, M. E., MacLeod, A. M., Snyder, A. Z., Powers, W. J., Gusnard, D. A., & Shulman, G. L. (2001). A default mode of brain function. *Proceedings of the National Academy of Sciences of the United States of America*, *98*, 676–682.

Rostrup, E., Law, I., Blinkenberg, M., Larsson, H. B., Born, A. P., Holm, S., & Paulson, O. B. (2000). Regional differences in the CBF and BOLD responses to hypercapnia: A combined PET and fMRI study. *NeuroImage*, *11*, 87–97.

Rubinov, M., & Sporns, O. (2010). Complex network measures of brain connectivity: Uses and interpretations. *NeuroImage*, *52*, 1059–1069.

Salvador, R., Suckling, J., Coleman, M. R., Pickard, J. D., Menon, D., & Bullmore, E. (2005). Neurophysiological architecture of functional magnetic resonance images of human brain. *Cerebral Cortex*, *15*, 1332–1342.

Sporns, O. (2012). *Discovering the human connectome*. Cambridge, MA: MIT Press.

Sporns, O., & Betzel, R. F. (2016). Modular brain networks. *Annual Review of Psychology*, *67*, 613–640.

Sporns, O., & Zwi, J. D. (2004). The small world of the cerebral cortex. *Neuroinformatics*, *2*, 145–162.

Stam, C. J., Jones, B. F., Nolte, G., Breakspear, M., & Scheltens, P. (2007). Small-world networks and functional connectivity in Alzheimer's disease. *Cerebral Cortex*, *17*, 92–99.

Sun, J., Liu, Z., Rolls, E. T., Chen, Q., Yao, Y., Yang, W., … Qiu, J. (2019). Verbal creativity correlates with the temporal variability of brain networks during the resting state. *Cerebral Cortex*, *29*, 1047–1058.

Tettamanti, M., Paulesu, E., Scifo, P., Maravita, A., Fazio, F., Perani, D., & Marzi, C. A. (2002). Interhemispheric transmission of visuomotor information in humans: fMRI evidence. *Journal of Neurophysiology*, *88*, 1051–1058.

van den Heuvel, M. P., Mandl, R. C., Stam, C. J., Kahn, R. S., & Hulshoff Pol, H. E. (2010). Aberrant frontal and temporal complex network structure in schizophrenia: A graph theoretical analysis. *The Journal of Neuroscience*, *30*, 15915–15926.

Wang, J., Ren, Y., Hu, X., Nguyen, V. T., Guo, L., Han, J., & Guo, C. C. (2017). Test–retest reliability of functional connectivity networks during naturalistic fMRI paradigms. *Human Brain Mapping*, *38*, 2226–2241.

Wang, J., Yang, Z., Zhang, M., Shan, Y., Rong, D., Ma, Q., … Lu, J. (2019). Disrupted functional connectivity and activity in the white matter of the sensorimotor system in patients with pontine strokes. *Journal of Magnetic Resonance Imaging*, *49*, 478–486.

Watts, D. J., & Strogatz, S. H. (1998). Collective dynamics of 'small-world' networks. *Nature*, *393*, 440–442.

Westerhausen, R., & Hugdahl, K. (2008). The corpus callosum in dichotic listening studies of hemispheric asymmetry: A review of clinical and experimental evidence. *Neuroscience and Biobehavioral Reviews*, *32*, 1044–1054.

Wig, G. S. (2017). Segregated systems of human brain networks. *Trends in Cognitive Sciences*, *21*, 981–996.

Wu, G. R., Liao, W., Stramaglia, S., Ding, J. R., Chen, H., & Marinazzo, D. (2013). A blind deconvolution approach to recover effective connectivity brain networks from resting state fMRI data. *Medical Image Analysis*, *17*, 365–374.

Wu, G. R., & Marinazzo, D. (2016). Sensitivity of the resting-state haemodynamic response function estimation to autonomic nervous system fluctuations. *Philosophical Transactions. Series A, Mathematical, Physical, and Engineering Sciences*, *374*, 20150190.

Wu, T. L., Wang, F., Li, M., Schilling, K. G., Gao, Y., Anderson, A. W., … Gore, J. C. (2019). Resting-state white matter-cortical connectivity in non-human primate brain. *NeuroImage*, *184*, 45–55.

Wu, X., Yang, Z., Bailey, S. K., Zhou, J., Cutting, L. E., Gore, J. C., & Ding, Z. (2017). Functional connectivity and activity of white matter in somatosensory pathways under tactile stimulations. *NeuroImage*, *152*, 371–380.

Zalesky, A., Fornito, A., Harding, I. H., Cocchi, L., Yucel, M., Pantelis, C., & Bullmore, E. T. (2010). Whole-brain anatomical networks: Does the choice of nodes matter? *NeuroImage*, *50*, 970–983.

SUPPORTING INFORMATION

Additional supporting information may be found online in the Supporting Information section at the end of this article.

How to cite this article: Li J, Biswal BB, Wang P, et al. Exploring the functional connectome in white matter. *Hum Brain Mapp*. 2019;40:4331–4344. https://doi.org/10.1002/hbm.24705